Article

Study on the Failure Process and Acoustic Emission Characteristics of Freeze–Thawed Sandstone under Cyclic Loading and Unloading

Chaoyun Yu [1,2], Shenghui Huang [1], Junkun Li [1], Xiangye Wu [3,*], Yuhang Tian [3] and Xiankai Bao [1]

[1] School of Civil Engineering, Inner Mongolia University of Science and Technology, Baotou 014010, China; yuchaoyun1989@163.com (C.Y.); 15039770160@163.com (S.H.); 15673530306@163.com (J.L.); bxkzlm@163.com (X.B.)

[2] Inner Mongolia Autonomous Region Key Laboratory of Civil Engineering Safety and Durability, Baotou 014010, China

[3] Institute of Mining and Coal, Inner Mongolia University of Science and Technology, Baotou 014017, China; 15031137434@163.com

[*] Correspondence: 2019712@imust.edu.cn; Tel.: +86-159-9864-2276

Abstract: In order to investigate freeze–thawed red sandstone failure processes under cyclic loading and unloading conditions, real-time acoustic emission (AE) and scanning electron microscopy (SEM) techniques were used to reveal the fracture process of the saturated red sandstone after cyclic loading and unloading tests using uniaxial compression. The results show that the stress–strain curves of the freeze–thawed sandstones show signs of hysteresis and exhibit a two-stage evolution of "sparse → dense". In the cyclic loading and unloading process, the modulus of elasticity in the loading process is always larger than that in the unloading process, while the Poisson's ratio is the opposite, and the radial irreversible strain and cumulative irreversible strain are larger than those in the axial direction. As the number of freeze–thaw cycles increases, the rock specimens need more cycles of loading and unloading to make the crack volume compressive strain $\Delta \varepsilon_{cv}^{+}$ reach the maximum value and tend to stabilize, while the crack volume extensional strain $\Delta \varepsilon_{cv}^{-}$ tends to decrease gradually. This study also shows that the growth phase of the cyclic loading and unloading process has more ringing counts and a shorter duration, while the slow degradation phase has more ringing counts with loading and less with unloading. In addition, the F-T cycle gradually changes the internal microcracks of the red sandstone from shear damage, which is dominated by shear cracks, to tensile damage, which is dominated by tensile cracks. This study's findings contribute to our knowledge of the mechanical characteristics and sandstone's degradation process following F-T treatment, and also serve as a guide for engineering stability analyses conducted in the presence of multiphysical field coupling.

Keywords: rock mechanics; cyclic loading and unloading; freeze-thaw cycle; acoustic emission

1. Introduction

Rock mass engineering refers to any engineering activities performed or structures built inside or on the surface of a rock mass, including the mining of mineral resources, utilization of water resources, construction of railway tunnels, prevention and control of geological disasters, etc. [1–3]. In engineering practice, the primary subject of investigation is rock mass stability. Because of the complexity and variety of the natural environment, the natural rock materials' mechanical and physical characteristics vary depending on the external environmental circumstances, such as temperature [4,5], freeze-thaw (F-T) cycles [6–8], osmotic pressure [9], and saturation [10]. Of all the variables, freeze–thaw cycles have a significant impact on the mechanical and physical characteristics of rocks. F-T cycles are a significant element impacting the safe and effective operation of engineering

structures, particularly in the fields of mineral resource extraction and railway tunnel building in alpine locations [11–13]. Water from rainfall or snowmelt penetrates geological discontinuities in the rock mass, such as laminar planes, cracks, joints, and faults, and when the outside ambient temperature is below freezing, water freezes in the rock mass pores. Due to the phase transition of water to ice, its volume increases by 9–10%, which correspondingly generates an enormous frost heave force [14,15]. Frost heave forces promote the expansion of new microfissures, thus causing great damage to rock engineering structures. In addition, the rock mass in many railway tunnels and mining projects is always subject to complex cyclic loading and unloading (such as excavation and support of underground chambers, blasting vibration, and train load of highway tunnels). Estimating the stability of rock engineering over the long run in cold places thus requires an understanding of the mechanical characteristics of F-T cycles and the cyclic loading and unloading of rocks in these regions [16,17].

Thus far, in order to demonstrate how F-T cycles affect the mechanical characteristics of rock, a series of experiments have been carried out, and important results have been achieved. At a macroscopic level, Momeni et al. [18] chose three distinct varieties of Alvand granitoid rocks for freeze–thaw experiments on a macroscopic basis. The uniaxial compressive strength (UCS), tensile strength, P-wave velocity, and dry density all drop with an increase in the number of F-T cycles, although porosity and water absorption increase. Zhang et al. [19] conducted split-tensile tests on rocks after F-T cycles and reported that the deterioration modes of rocks were spalling mode, fracture mode, and crack mode. At a microscopic level, Chen et al. [20] used NMR to find that under freeze–thawing, the red sandstone showed a gradual trend from the growth of small pores to the co-growth of medium and large pores. Lu et al. [21] used SEM to observe the fine morphological features of mudstone fractures and elucidate the fine-scale damage rupture mechanism of mudstone under the action of F-T cycles. These researchers determined that the fine-scale rupture of mudstone with a lower number of F-T cycles was a brittle fracture; however, mudstone with a higher number of F-T cycles locally revealed significant ductile damage characteristics. Because it can reflect and track the growth and propagation of cracks in rock masses in real time, acoustic emission (AE) is a frequently used real-time nondestructive monitoring technology that is frequently used in test and engineering sites to monitor the damage evolution process of coal and rock masses [22,23]. For instance, Zhang et al. [24] performed shear experiments on rocks subjected to varying freeze–thaw cycles and found that these cycles attenuated the variations in AE signal characteristics at various shear process phases. Li et al. [25] conducted a uniaxial compression cyclic load test on rocks and determined that in the loading and unloading test, the AE count rate exhibited a steady upward trend with an increasing number of cycles but increased sharply during the last cycle. Song et al. [26] tested limestone exposed to freeze–thaw cycles using a uniaxial AE method. These scholars determined that with increasing freeze-thaw times, AE signals were active and presented local high-density release characteristics, and the b value revealed a "V"-type change. Chu et al. [27] found that the freezing and freeze-thawing of LN_2 did not change the AE event period of coal samples during uniaxial loading, but the loudest emission count and cumulative count of coal samples gradually decreased with increasing freezing time and freeze-thawing times. Regarding the damage model, Feng et al. [28] developed an F-T damage model based on the relative change in the energy dissipation ratio prior to and following freeze–thaw cycling. Uniaxial compressive strength and peak strain were used to assess the damage model's correctness. Zhang et al. [29] established a constitutive equation by using F-T damage as the initial damage state of rocks. Using this equation, the damage evolution and macroscopic damage behavior of the microstructure of rock material can be well described. By PFC numerical simulation, Feng et al. [28] established the functional relationship between meso-scale parameters and the number of F-T cycles. A comparison was made between the numerical simulation and actual results in order to confirm the validity of the numerical method for simulating the uniaxial compression of saturated sandstone following F-T cycles. It is clear that scholars have produced a wealth

of research results on freeze–thawed rocks under uniaxial compression conditions in terms of macroscopic or fine-scale damage modeling and numerical simulation.

However, loads may be loaded and unloaded from rocks several times in real-world engineering applications. For example, in underground mining, a particular rock structure may experience cyclic disturbance due to the cyclic load created by blasting. In open-pit mining, when the rock slope is continuously excavated, the stress magnitude changes; that is, cyclic stress can cause cumulative rock damage and subsequently change the rock structure, resulting in the eventual failure of the rock mass [30,31]; cyclical loading and unloading on a railroad or highway causes an increase or decrease in the load-bearing capacity. Scholars have primarily investigated rock materials at room temperature or under uniaxial compression; however, there has been little research on the mechanical properties of F-T rocks under cyclic loading and unloading situations. For this reason, under cyclic loading and unloading conditions, the deformation and fracture characteristics of saturated red sandstone with various F-T cycles were examined in this study. Real-time AE monitoring technology was used to monitor rock fracture events and extract the AE signal of the rock during cyclic loading and unloading to study its fracture mode. In addition, the process of rock F-T damage was visualized using SEM scanning technology to better understand the influence of F-T cycles on rock damage. The research results provide theoretical guidance for mineral resource development and engineering stability analysis under coupled multiphysics conditions.

2. Experimental Methods

2.1. Sample Preparation

The sandstone samples that were used in the cyclic loading and unloading testing were from an open-pit slope in Ordos City, China's Inner Mongolia Autonomous Region, where winter lows can drop as low as minus 27 °C. The elemental composition of the red sandstone was determined by using energy-dispersive X-ray spectroscopy (EDS) analysis (Figure 1), and the main elements were O (54.9%), Si (26.8%), Fe (5.7%), Ca (5.7%), Al (4.54%), K (1.71%), and Mg (0.65%). Red sandstone has an elastic modulus of 18.2 GPa, a UCS of 68.77 MPa, and a density of 2.76 g/cm^3 in its natural state. In compliance with the guidelines provided by the International Society of Rock Mechanics (ISRM) [32], the rock mass was formed into a cylinder 100 mm in length and 50 mm in diameter. The samples were further cut and polished to ensure that the nonuniformity inaccuracy was under 0.05 mm and the ratio of parallelism was less than 0.1 mm.
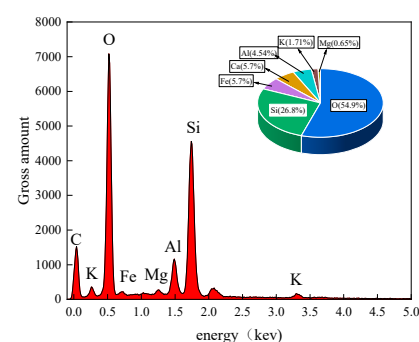

Figure 1. EDS energy spectrum of red sandstone.

2.2. Test Equipment and Process Steps

The cyclic loading and unloading test equipment and detailed procedures for F-T sandstone are summarized as follows:

(1) The prepared red sandstone samples were first vacuum-saturated with a vacuum saturation device for 24 h to fully saturate the specimens, and then a cryogenic refrigerator was used to achieve the freeze-thaw cycle, as shown in Figure 2. Referring to earlier research [29,33–35], it was determined that the freeze–thaw temperature and time ranges

of sandstone should be −20 °C~20 °C and 12 h, respectively, in order to more thoroughly research the mechanical characteristics of rocks that have undergone F-T processing. The saturated specimens were frozen for 12 h in a low-temperature refrigerator. After that, they were taken out and put into a water bath that was set to 20 °C (Figure 2); this process is regarded as one F-T cycle. Figure 2 displays a thorough F-T program. Four groups of sandstone samples were created, and three specimens were chosen from each group to undergo 0, 5, 15, and 20 freeze–thaw cycles. Additionally, the rock samples were first chopped into lengths of less than 2 cm and thicknesses of less than 0.5 cm in order to analyze their micromorphological features following various freeze–thaw cycle treatments. Then, the cut samples were subjected to freeze-thaw treatments, and the samples were scanned using SEM after these treatments. The test samples are shown in Figure 2.

(2) The freeze-thawing-treated specimens were placed on an HUT-106 universal test machine for uniaxial cyclic loading test with a maximum loading load of 1000 kN, as shown in Figure 2. Axial loading was adopted at a loading rate of 500 N/S. During the cycle of loading and unloading, appropriate upper and lower weights were chosen based on the compressive strength of red sandstone at various freezing and thawing timeframes.

(3) During the test, the microfracture signal was continuously monitored using the PAC AE system. Eight probes were deployed, the acquisition frequency was 10 Hz, the threshold value was 50 dB, and the prerelease gain was 40 dB. During the test, a BZ2205C static resistance strain gauge was used to continuously monitor the axial and radial strains (Figure 2). The upper and lower ends of the test specimen connected to the axial and radial strain gauge were smeared with a small amount of petroleum jelly and placed on the AE probe based on the press. The four probes, upper and lower, were symmetrically positioned. The probes were linked to the sensor and amplifier in the appropriate order before being connected to the control system. Figure 2 depicts the loading and monitoring system.

(4) According to the upper and lower loads obtained in step (2), the load path was set as follows: 0→50 kN→100 kN→50 kN→100 kN→... → peak stress. The stress cycle was repeated 10 times or until specimen failure. Figure 2 displays the specific cyclic loading and unloading path.

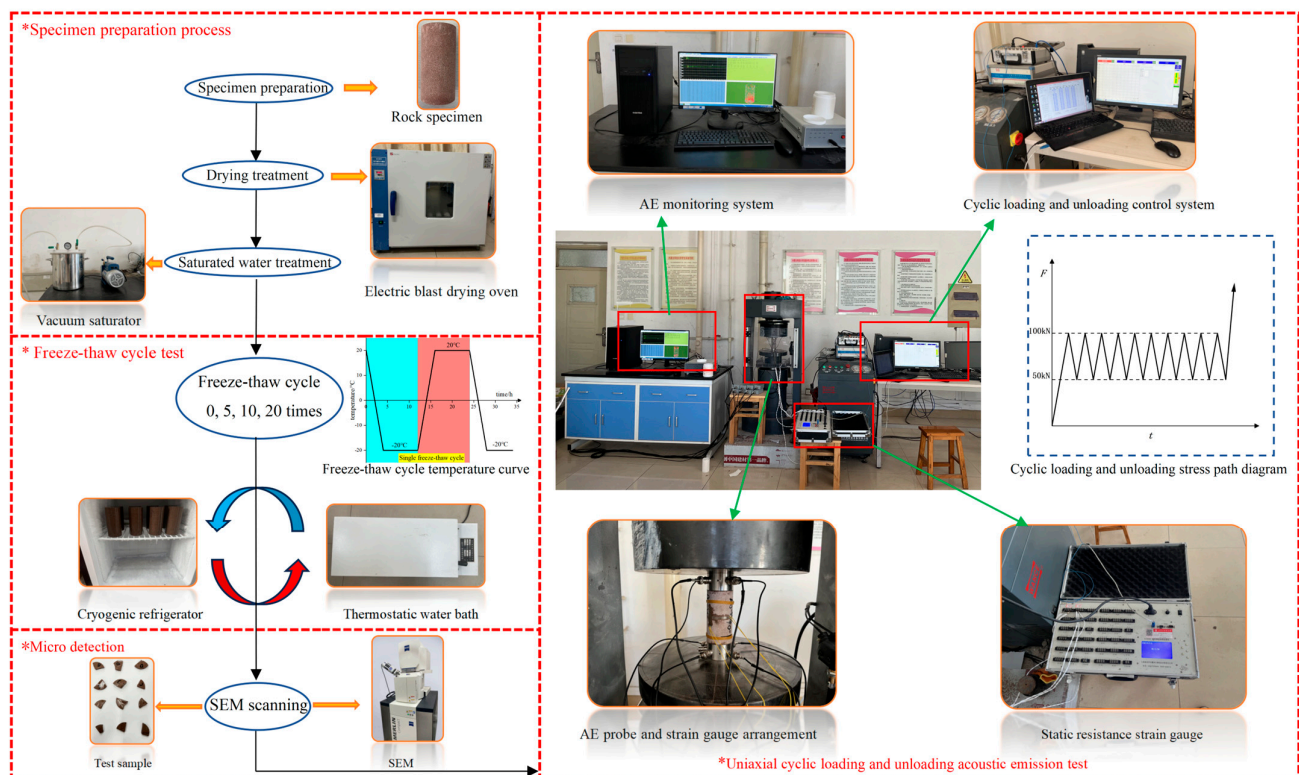**Figure 2.** Arrangement of test equipment and experimental apparatus.

3. Results and Discussion

3.1. Stress-Strain Curve Characteristics during Cyclic Loading and Unloading

During uniaxial cyclic loading and unloading, the volume of rock varies primarily as a result of reversible and irreversible deformation. When stress is removed, some of the rock is restored to its original state, i.e., before deformation. This is referred to as elastic deformation, which is a reversible process. In contrast, some of the rock cannot be restored after unloading. This is called plastic deformation, which is irreversible. Figure 3a–d show the usual stress–strain curves from rock cyclic loading and unloading tests under different freeze–thaw intervals. From Figure 3, with increasing cyclic loading and unloading times, the stress-strain curve shows two stages of "sparse (stage I) → dense (stage II)". This is because there is a clear hysteresis curve because irreversible deformation happens throughout each cycle of loading. Consequently, after every unloading, the rock's axial deformation cannot restore to its initial strain value. The relationship between axial strain, reversible strain, and irreversible strain is as follows [4]:

$$\varepsilon_N = \varepsilon_N^r + \varepsilon_N^e \tag{1}$$

$$\sum \varepsilon_N^r = \varepsilon_1^r + \varepsilon_2^r + \ldots + \varepsilon_N^r \tag{2}$$

where N represents the Nth cycle of loading and unloading; ε_N, ε_N^e, and ε_N^r are the total, reversible, and irreversible strains generated during the *Nth* loading cycle, respectively; and the total irreversible strain produced during the loading and unloading cycles is represented by ε_N^r.
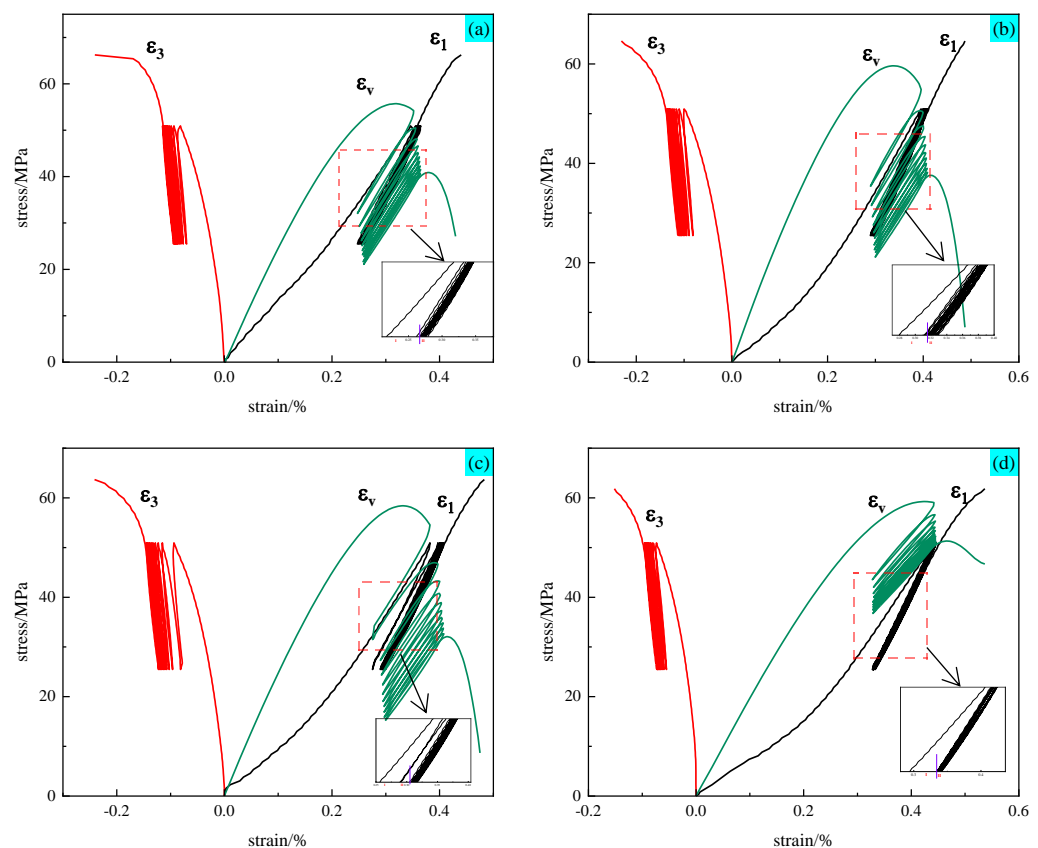

Figure 3. Normal stress–strain curves for cyclic loading and unloading of rocks with varying numbers of F-T cycles are as follows: (**a**) 0; (**b**) 5; (**c**) 10; and (**d**) 20 times.

Equations (1) and (2) are utilized to compute the axial and radial irreversible strain as well as the axial and radial cumulative unstrain under various freezing and thawing conditions during rock cyclic loading and unloading, as seen in Figure 4. The results indicate that the axial and radial irreversible strains of the rock sample first increase, then rapidly decrease, and finally slowly stabilize. On the other hand, the cumulative irreversible strain rises quickly at first, then climbs gradually, and finally stabilizes gradually. This is because the rock specimen has more pore joints prior to loading and unloading, and following the initial loading and unloading cycle, the specimen's irreversible strain reaches its maximum value. As the number of loading and unloading cycles increases gradually, the specimen is gradually compacted, the deformation gradually becomes stable, and the irreversible strain steadily becomes stable from a slow increase. A certain amount of loading and unloading cycles causes the specimen's damage to progressively worsen. The specimen's damage and the total irreversible strain reach their maximum after ten loading and unloading cycles.
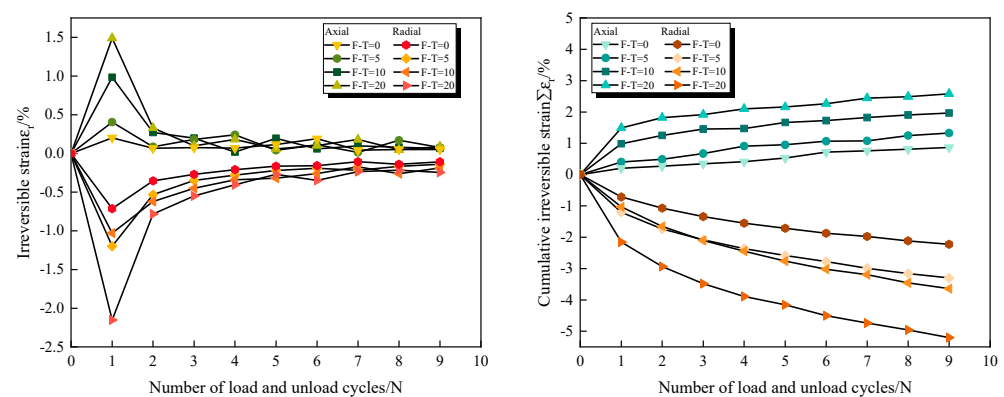

Figure 4. Irreversible strain and cumulative irreversible strain under cyclic loading and unloading.

In addition, the F-T cycles have a greater effect on the irreversible deformation of the rock specimens. It is clear from Figure 4 that the specimen's cumulative irreversible strain reaches its highest value after 20 cycles of freezing and thawing. As the frequency of freezing and thawing cycles rises, the irreversible strain likewise steadily increases. This is due to the fact that the internal pore defects of saturated rocks are filled with water during the F-T cycle, which generates freezing and expansion forces, leading to the continuous expansion and development of internal pore joints. This is in agreement with the findings of Song et al. [26], Liu et al. [36], and Niu et al. [37]. The deformation of the rock increases continuously, and the resulting irreversible strains also increase gradually. Moreover, Figure 4 illustrates that when loading and unloading in cycles, the irreversible strain in the radial direction and the cumulative irreversible strain are greater than those in the axial direction due to the absence of a binding force (supporting force) in the radial direction of the rock.

3.2. Elastic Modulus (E) and Poisson's Ratio (μ) during Cyclic Loading and Unloading

Two crucial metrics for assessing the progressive breakdown process of rock are the elastic modulus (E) and Poisson's ratio (μ). These parameters affect the deformation ability of the material. The material is more stiff and has a poorer deformation ability the higher its elastic modulus. The material's radial strain increases with increasing Poisson ratio. Examining the elastic modulus change law and Poisson's ratio during cyclic loading and unloading is essential to understanding the deformation properties of red sandstone. The elastic modulus and Poisson's ratio are calculated as follows [4]:

$$E = \frac{\sigma_{1min} + 50\%(\sigma_{1max} - \sigma_{1min})}{\varepsilon_{1min} + 50\%(\varepsilon_{1max} - \varepsilon_{1min})} = \frac{\sigma_{1max} + \sigma_{1min}}{\varepsilon_{1max} + \varepsilon_{1min}} \tag{3}$$

$$\mu = \frac{\varepsilon_{1min} + 50\%(\varepsilon_{1max} - \varepsilon_{1min})}{\varepsilon_{3min} + 50\%(\varepsilon_{3max} - \varepsilon_{3min})} = \frac{\varepsilon_{1max} + \varepsilon_{1min}}{\varepsilon_{3max} + \varepsilon_{3min}} \tag{4}$$

where E is the elastic modulus (MPa), μ is Poisson's ratio, and σ_{1max} and σ_{1min} are the maximum and minimum axial stresses (MPa) during each cycle of loading and unloading, respectively. ε_{1max}, ε_{1min} and ε_{3max}, ε_{3min} are the axial and radial strains corresponding to σ_{1max} and σ_{1min}, respectively. Based on Equations (3) and (4), the samples subjected to varying freeze–thaw periods were measured for elastic modulus (E) and Poisson's ratio (μ), as depicted in Figure 5.
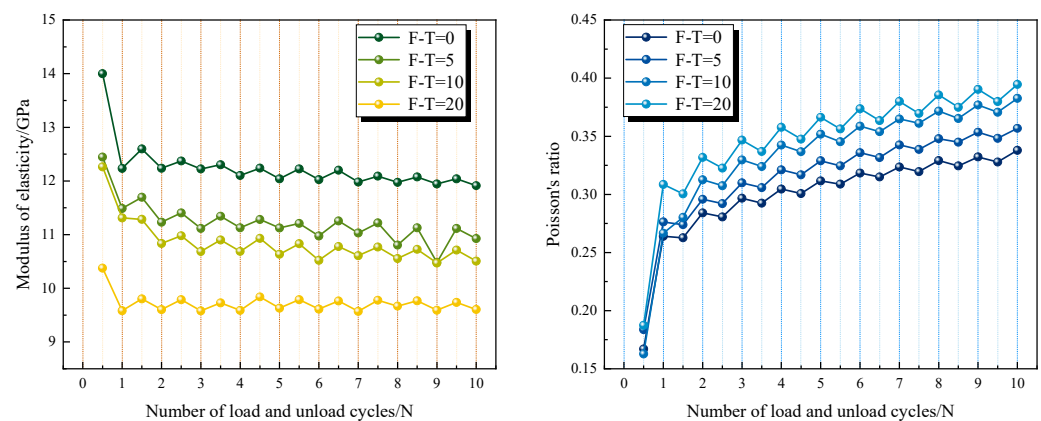

Figure 5. Comparison between the elastic modulus value and Poisson's ratio during rock cyclic loading and unloading after different F-T cycles.

The loading process's elastic modulus is always significantly higher than the unloading process's in each cycle of the loading and unloading process under different freeze–thaw intervals, as shown by Figure 5, which also shows significant variations in the first two cyclic loading and unloading processes. This is because the specimen has pores in it. The cyclic loading process of a specimen is actually a process of gradually compressing the pores and increasing the density of the rock. Both reversible and irreversible deformation occur when something is loaded. The deformation that occurs during the unloading process is only reversible elastic deformation; in actuality, the specimen is being unloaded in a manner that restores the loading deformation. As a result, the loading process has a much higher elastic modulus than the unloading process. A significant amplitude of change is noticed in the first two cycles of the loading and unloading process under different freeze–thaw intervals. Poisson's ratio is consistently lower in each cycle than in the unloading phase. This stands in stark contrast to the elastic modulus's changing trend over the loading and unloading process.

Moreover, the rock specimen's elastic modulus increases and Poisson's ratio gradually drops with increased cyclic loading and unloading times before finally tending to be stable. Because the rock specimens have more internal pores during the first two loading and unloading operations than during the later stages, there is a significant change in the elastic modulus and Poisson's ratio. According to the test results above, the rock specimen becomes denser and its material strength is somewhat increased prior to the rock specimen failing as a result of the rock's pore structure being adjusted during the cyclic loading and unloading process. Among them, the strengthening effect of the first two cycles in unloading is more obvious. Research by Li et al. [38] and Xiao et al. [4] indicates that cyclic loading and unloading tests enhance sandstone materials in a certain way. This is in line with their findings.

Lastly, Figure 5 also demonstrates how the elastic modulus of each cycle loading and unloading process declines with a rise in the quantity of F-T periods, reaching its lowest value at 20 cycles. The Poisson's ratio rises as the number of freeze–thaw cycles increases. This conclusion is consistent with the research results of Fu et al. [39]. This is because the pore water inside the rock specimen freezes during the F-T cycle, creating frost heave stresses, and the pores inside the specimen grow and widen. When the external water enters the new pores during melting, the damage is further increased, resulting in an overall decrease in the elastic modulus of the rock specimen under cyclic loading and unloading. The porosity of the rock specimen is well developed in the process of F-T, which increases its deformation ability, so Poisson's ratio of the rock specimen is generally increased.

3.3. Crack Volume Evolution Law of Freeze-Thaw Rock under Cyclic Loading and Unloading

Rock is a kind of heterogeneous body containing mesostructural defects such as cracks, joints, and pores [40]. When affected by F-T cycles, pores, joints, and cracks in rock materials change significantly [28]. In the process of axial loading of rock under freeze-thaw action, the pores and cracks in rock specimens are gradually compressed and closed with increasing stress, and the crack volumetric strain is gradually reduced. The pore joint that is present in the rock specimen is compacted when the stress is greater than the rock's initial fracture stress. When the stress is continuously applied, new cracks gradually appear in the rock specimen, and the crack volumetric strain gradually increases [41]. The internal crack of the rock specimen is compressed during loading in the cycle of loading and unloading. As a result of the rock specimen's elastic–plastic characteristics, the inner portion of the specimen regains its crack shape and its elastic deformation portion returns. Crack compression, partial recovery, and the processes of crack initiation and propagation are all included in cyclic loading and unloading. Thus, under various freeze–thaw cycles, it is imperative to investigate the dynamic evolution law of fracture volumetric strain during cyclic rock loading and unloading [42].

3.3.1. Crack Volumetric Strain Calculation

This section examines the variations in rock specimens' volumetric and elastic volumetric strains during each loading procedure. The crack volumetric strain method was first proposed by Martin et al. [43] and has since been widely used. The specific calculation method is as follows:

$$\begin{cases} \varepsilon_v = \varepsilon_1 + \varepsilon_2 + \varepsilon_3 = \varepsilon_{ev} + \varepsilon_{cv} \\ \varepsilon_{ev} = \frac{1-2\mu}{E}(\sigma_1 + \sigma_2 + \sigma_3) \\ \varepsilon_{cv} = \varepsilon_v - \varepsilon_{ev} = \varepsilon_v - \frac{1-2\mu}{E}(\sigma_1 + \sigma_2 + \sigma_3) \end{cases} \tag{5}$$

where E is the elastic modulus, GPa; μ is Poisson's ratio; ε is the major strain corresponding to σ; and the rock's total volumetric strain, elastic volumetric strain, and fracture volumetric strain are represented, respectively, by ε_v, ε_{ev}, and ε_{cv}.

This test is uniaxial compression, $\sigma_2 = \sigma_3 = 0$, and the volumetric strain of the crack is defined as follows:

$$\varepsilon_{cv} = \varepsilon_v - \varepsilon_{ev} = \varepsilon_v - \frac{1-2\mu}{E} \bullet \sigma_1 \tag{6}$$

Equation (6) allows for the calculation of the rock specimen's crack volumetric strain under various F-T conditions. Crack compression and crack propagation are two processes that go hand in hand with the loading process [4]. The crack volumetric strain diagram throughout the loading process is constructed, as illustrated in Figure 6, in order to completely analyze the internal crack volumetric strain and crack expansion volumetric strain of the rock specimen during each loading operation. The maximum compression point occurs throughout each loading phase and is determined by the maximum fracture volumetric strain point. During every loading procedure, when the crack volumetric strain curve reaches compression point C, the change in crack volumetric strain is expressed as $\Delta\varepsilon_{cv}^{+}$. This illustrates how rock behaves during the current loading stage when subjected to

various cyclic loads. Its value represents the strength of the restorability of the crack volume deformation of a rock specimen after cyclic loading. The crack expands and the volumetric strain starts to diminish when the stress levels are above the original crack stress. The crack growth volume changes from point C to the end, and the crack growth volumetric strain change is represented by the symbol $\Delta\varepsilon_{cv}^{-}$ (where the negative sign indicates expansion and the crack volume growth is the cause of the change in $\Delta\varepsilon_{cv}^{-}$). This parameter shows the rock specimen's crack propagation characteristics at the current loading stage following various cyclic loads. Its value indicates how strong the fracture growth potential is following cyclic loading in the preceding cycle. Figure 6 displays the results of the computation of $\Delta\varepsilon_{cv}^{+}$ and $\Delta\varepsilon_{cv}^{-}$.
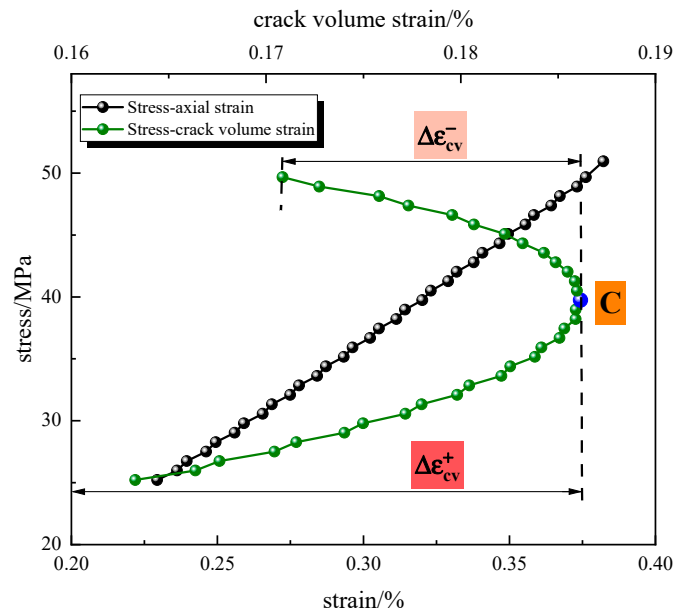

Figure 6. Calculation of $\Delta\varepsilon_{cv}^{+}$ and $\Delta\varepsilon_{cv}^{-}$.

3.3.2. Analysis of the Crack Volumetric Strain Law

Figure 7 illustrates the results of the aforesaid calculation technique for $\Delta\varepsilon_{cv}^{+}$ and $\Delta\varepsilon_{cv}^{-}$ in the cyclic loading and unloading of freeze–thawed sandstone. In the initial two cyclic loading and unloading procedures, $\Delta\varepsilon_{cv}^{+}$ exhibits a rapid growth rate, represented by a linear increase (I). Following the second loading and unloading cycle, there was a modest growth trend as indicated by the slow growth rate of $\Delta\varepsilon_{cv}^{+}$ (II). Following the fourth to seventh loading and unloading cycles, $\Delta\varepsilon_{cv}^{+}$ reaches its maximum value. Subsequently, it enters a stable period (III), and $\Delta\varepsilon_{cv}^{+}$ is basically unchanged until the end of the 10th loading and unloading cycle. As a result, when cyclic loading and unloading times increase, $\Delta\varepsilon_{cv}^{-}$ falls. The variation in $\Delta\varepsilon_{cv}^{+}$ and $\Delta\varepsilon_{cv}^{-}$ in freeze-thawed and non-freeze-thawed rock samples is generally consistent.

Freeze-thaw action will change the crack distribution and pore joint development characteristics of rock specimens. Rocks with varying initial pore junctions will exhibit distinct crack volumetric strain evolution characteristics following varying numbers of F-T cycles [44]. Natural rock without F-T cycles has some defects. After it is filled with water, the external water source fills the pore joints of the rock. The water–ice phase change inside the rock specimen causes frost heave force during an F-T cycle. As seen by the SEM pictures in Figure 8, the number of pore flaws in the rock specimen increases as the number of F-T cycles increases progressively. Cracks also gradually expand and join. According to the SEM images of rock samples after different F-T treatments (Figure 8), combined with the results in Figure 7, the analysis is summarized as follows:

(1) Figure 7 shows that for rock specimens with fewer freezing and thawing cycles (0, 5), $\Delta\varepsilon_{cv}^{+}$ increased rapidly during loading and unloading in the first two cycles, reached the maximum value in the fourth cycle, and remained stable after that. The rock specimen with 10 or 20 F-T cycles had a rapid increase in its $\Delta\varepsilon_{cv}^{+}$ value in the first 2 cycles. In the sixth cycle, the specimen with ten F-T cycles reached its maximum value, and in the seventh cycle, the specimen with twenty freeze–thaw cycles even reached its maximum value and remained stable. This is because the F-T cycle causes the rock specimen to sustain more damage and widens its internal pores and fissures.

Based on the SEM examination of Figure 8a,b, compared with non-freeze-thaw exposure, the pores and cracks of red sandstone samples exhibit little difference in development degree at low F-T times (0, 5), and only large "pit"-type pores exist locally. The features of the pore structure gradually emerge when the number of F-T cycles rises to 10, as demonstrated by Figure 8c, where the pores and cracks created by the cycles are interconnected. According to Figure 8d, at 20 cycles of freeze–thaw, "pit"-type pores and cracks interpenetrate to generate a large zone of F-T damage, and the maximum values of pore size, crack length, and connectedness are reached [45]. Therefore, the majority of the fissures in the specimen's compressible pore space were compacted following the first two cycles of loading and unloading. Compared with the specimens with fewer F-T cycles (0, 5), the porosity and nascent cracks of the rock specimens with more F-T cycles (10, 20) increased significantly, and the "pit"-type pores were connected with the cracks, requiring more cycles to close the internal gaps of the specimens. Therefore, after 6~7 cycles of loading and unloading with more freezing and thawing cycles (10, 20), $\Delta\varepsilon_{cv}^{+}$ reaches the maximum value.

(2) The specimen's compressible pore fractures were mostly crushed following the preceding cyclic loading and unloading. After unloading, the rock particles' stiffness reverted to their initial state. Consequently, some stiff particles' edge cracks progressively healed to go on to the following cyclic loading process. As demonstrated in Figure 5, the research outcomes above indicate that freeze–thaw cycles have an impact on the rock specimens' elastic modulus during cyclic loading and unloading. When there were fewer F-T cycles (0, 5), as opposed to more (10, 20), the rock particles showed better resistance to deformation, the elastic modulus was higher, and the rock specimen's deformation could be more effectively restored to its initial state following cyclic loading. Therefore, after four cycles of loading and unloading, $\Delta\varepsilon_{cv}^{+}$ basically remained unchanged. When there were more F-T cycles (10, 20), compared to fewer F-T cycles (0, 5), the deformation resistance and elastic modulus decreased. The compressible crack volume decreases during the subsequent loading cycle since most cracks cannot be fully recovered after each loading cycle. Consequently, $\Delta\varepsilon_{cv}^{+}$ can progressively become steady and unchanged after six to seven cycles of loading and unloading.

(3) The fractures in the rock specimen grew rapidly and joined because the axial stress was greater than the rock's damage stress. All things considered, rocks' damaging stress was roughly 70% of their peak stress [46]. In this test, the upper limit stress of cyclic loading and unloading was set at 50 MPa, and the corresponding stress level exceeded 70%, which belongs to the stage of unstable crack growth. Consequently, the volumetric strain curve of compressive fractures rose somewhat when cyclic loading and unloading started and the rock specimen's fissures started to widen. The pattern of crack growth in the sample varies when subjected to distinct F-T cycles [39]. As the number of F-T cycles increases, as illustrated in Figure 7, the $\Delta\varepsilon_{cv}^{-}$ values decrease progressively and are 0.62%, 0.53%, 0.42%, and 0.35%. As a result of the F-T action, the internal structure and physical characteristics of the rock were altered, influencing the crack's propagation mode and speed. In the unstable crack propagation stage, the rock specimen's crack volume shrank.
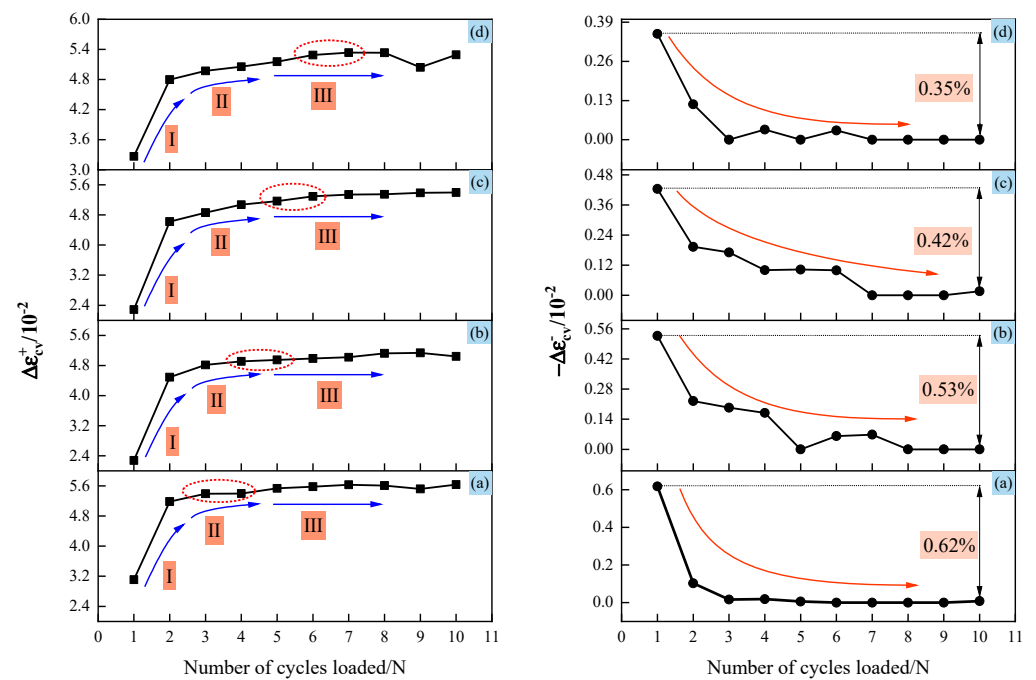
Figure 7. Volumetric strain in cracks during cyclic loading and unloading of rocks following varying F-T cycles: (**a**) 0; (**b**) 5; (**c**) 10; and (**d**) 20 times.
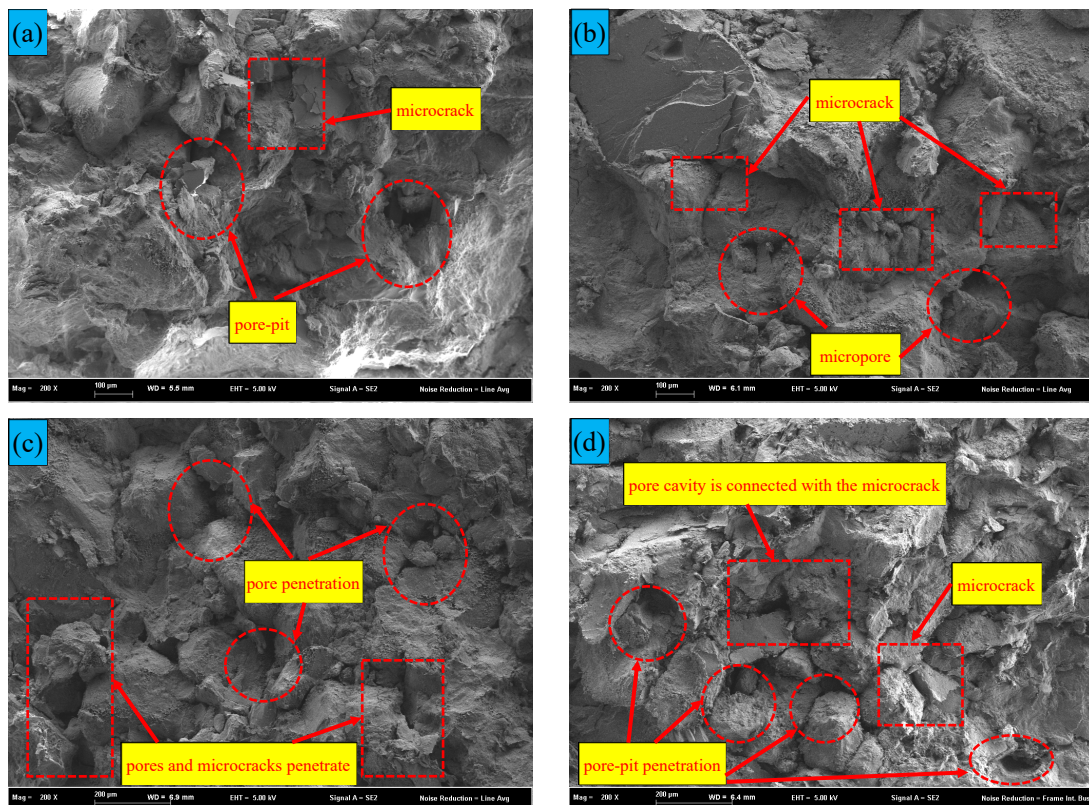

Figure 8. Microstructure of rock samples after different F-T cycles: (**a**) 0; (**b**) 5; (**c**) 10; and (**d**) 20 times.

4. Evolution Law of AE Characteristics during Cyclic Loading and Unloading

Numerous AE signals (such as ringing count, energy, amplitude, and frequency) are produced during uniaxial cyclic loading and unloading, and the macroscopic failure features of the rock specimens may be seen. When rocks are loaded and unloaded repeatedly, damage and failure characteristics can be accurately reflected in the AE signals that are produced [6,47]. Based on the ringing count and RA-AF value, the microcrack behavior of freeze–thawed sandstone during cyclic loading and unloading is examined in this section.

4.1. Law of Evolution for the Number of Rings during Recurrent Loading and Unloading

The "AE ringing count", which represents the number of vibration times of the ringing pulse over the predefined threshold signal in a unit of time, is a measure of the strength of the acoustic signal during the rock failure process and can reveal details about the characteristics of the damage to the rock brought on by the formation and enhancement of microscopic defects [47]. The curves of load, ringing count, cumulative ringing count, and cumulative ringing count of freeze–thawing red sandstone over time are displayed in Figure 9. These curves may be further classified into three stages: growth, slow decline, and steep increase. Furthermore, there is good consistency between the AE signal characteristics and the load curve during the entire cycle of loading and unloading.

(1) Growth stage (0~100 s)

The growth phase is when the cumulative number of rings and the number of bells in the specimen increases significantly as the load increases until the cyclic loading (100 s) begins. In this stage, there are more ringing counts, and the duration is short. This is because when the loading plate of the press and the rock specimen start to contact, there is a small amount of space between the specimen and the press. Under the action of inertia, the stress is too large instantaneously. Moreover, the specimen's preexisting pores are compressed during the first stage, which causes a notable rise in the ringing count and cumulative ringing count during that phase [48].

(2) Slow-down stage (100~2100 s)

During cyclic loading and unloading, the AE signals of sandstone exhibit comparable features under F-T cycles. The signals produced during the loading phase are primarily elastic waves caused by pore compaction and crack growth, which is why the ringing count rises with loading and falls with unloading. The signal generated in the unloading stage is mainly the friction force overcome by the compacted crack to restore the initial state [6]. The first cyclic loading and unloading generates intensive AE signals, and the cumulative ringing count reaches the maximum, while the subsequent cyclic loading and unloading only generates fewer AE signals, and the cumulative ringing count gradually decreases. This is a result of the first cyclic rock specimen's pores and cracks developing to their maximum value, while the specimen's internal structure gradually stabilizes and the damage grows more slowly with increased cycle loading and unloading times.

(3) Steep increase stage (2100 s~destruction)

The steepening phase is the continuous loading process after the end of the last loading and unloading cycle (2100 s), which generates a very small amount of AE signal. Because the interior cracks of the rock specimen are connected before the peak stress is achieved, a fracture network is gradually created, and the microfracture features are evident, the AE signal is greatly boosted when the load exceeds 100 kN. In addition, before the failure of F-T sandstone, there is a short AE signal silence period; that is, there is no loud emission activity in the short term. This can be used as a precursor criterion to predict the sudden failure of rock because the generation of the AE signal is the result of energy dissipation. Furthermore, in order for the rock to fully lose its bearing capacity during the loading process to the failure stage, enough elastic strain energy must build up to counteract the effects of particle dislocation and friction, which manifest as decreased AE activity.
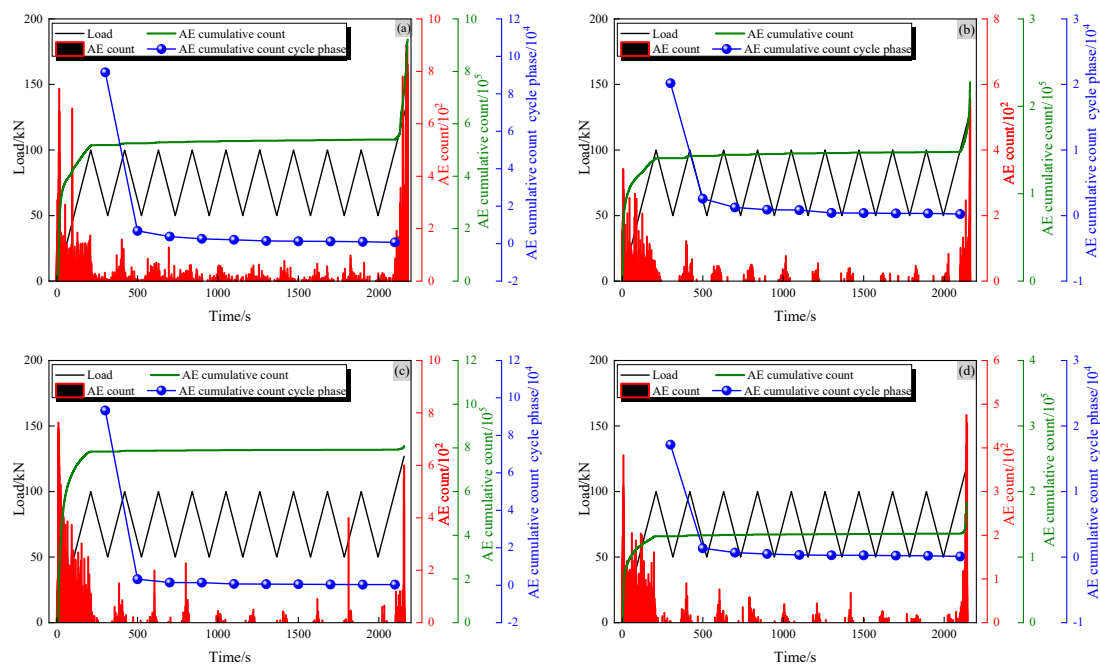
Figure 9. Evolution characteristics of the rock AE count and AE cumulative count after different F-T cycles: (**a**) 0; (**b**) 5; (**c**) 10; and (**d**) 20 times.

4.2. Evolution of Rupture Mode (RA-AF) during Cyclic Loading and Unloading

Cui et al. [41], Song et al. [47], and Niu et al. [49] suggested that the RA and AF indices of the AE parameters can be used to study the evolution of shear and tensile cracks in rocks.

Tensile cracks are characterized by high AF values and low RA values, composite cracks by low AF values and low RA values, and shear cracks by low AF values and high RA values. In red sandstone with varying F-T cycles, the distribution of microcrack types is depicted in Figure 10. The findings show that, for a given freeze–thawing frequency, there is minimal variation in the RA and AF particle distributions during each loading and unloading cycle. Notably, the first loading and unloading cycle exhibits the highest RA and AF particle density, as well as the most visible microcracks in the rock specimens. The type of microcracks inside the rock specimen is identified during the first loading and unloading cycle, and the distribution of RA and AF during the ensuing loading and unloading procedure is essentially in line with that of the first cycle.

Furthermore, as the quantity of F-T cycles rises, the internal microcracks in red sandstone can be seen in Figure 10. These cracks initially dominate shear failure, but over time, they shift to tensile failure, which is dominated by tensile cracks. The red sandstone with 0 F-T cycles is mainly characterized by shear microcracks, which form obvious weak shear planes through multiple penetrating cracks and cause the rock sample to show the characteristics of multicrack shear failure. The internal cracks in red sandstone after 5 F-T cycles are primarily shear and composite microcracks, which exhibit the features of macroscopic local shear failure of rock samples. Tensile and composite cracks make up the majority of the red sandstone's internal fractures after 10 F-T cycles, which is consistent with the macroscopic fracture failure characteristics of the rock samples. The red sandstone mostly displays a high number of tensile cracks after 20 F-T cycles, and these cracks demonstrate the features of multiple crack splitting and failure.
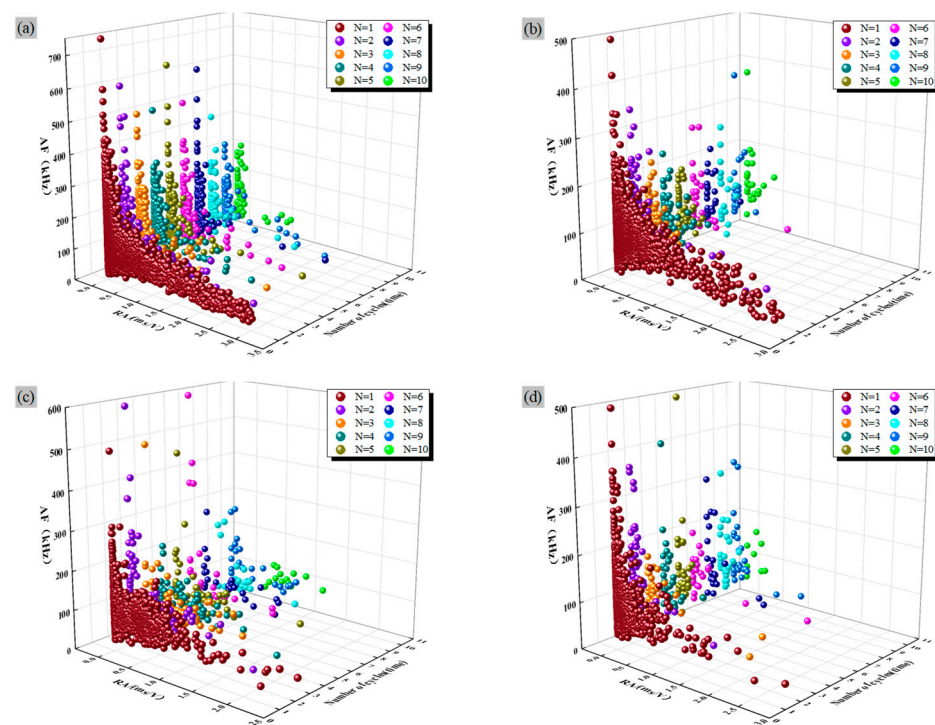
Figure 10. Rock ringing count evolution features and cumulative ringing count following varying F-T cycles: (**a**) 0; (**b**) 5; (**c**) 10; and (**d**) 20 times.

Most of the current studies on the mechanical properties and deterioration mechanisms of F-T rocks presuppose the F-T saturated state; however, natural rocks are often in the unsaturated state, and insufficient attention has been paid to rocks in different F-T and unsaturated states. Therefore, the coupling effects of different saturation levels and F-T cycling on the mechanical properties and AE characteristics of rocks will be investigated in the future.

5. Conclusions

Rocks' mechanical properties are significantly impacted by F-T cycles. This study uses saturated red sandstone that has undergone F-T treatment as its research subject, and it performs cyclic loading and unloading tests using uniaxial compression. The following is a summary of this paper's primary conclusions:

(1) A two-stage evolution typical of "sparse (first stage)→dense (second stage)" is shown in the hysteretic curve, with longer cyclic loading and unloading times because of the rock specimen's plastic deformation and pore compaction. The radial irreversible strain and cumulative irreversible strain surpass the axial strain after 20 freeze–thaw cycles, at which point the cumulative irreversible strain achieves its maximum value.

(2) The elastic modulus and Poisson's ratio are correlated with the number of F-T cycles during cyclic loading and unloading. The elastic modulus during loading is always greater than that during unloading, while Poisson's ratio during loading is always smaller than that during unloading. The elastic modulus of each cycle loading and unloading process falls as the number of F-T cycles grows, while Poisson's ratio increases. Both reach their respective extreme value when the number of freeze–thaw cycles reaches 20.

(3) During the cyclic loading and unloading process, there is a correlation between the volume compression and crack expansion and the number of F-T cycles. With an increasing number of F-T cycles, the rock specimen needs more cyclic loading and unloading to ensure that $\Delta\varepsilon_{cv}^{+}$ reaches the maximum value and becomes stable. The values of $\Delta\varepsilon_{cv}^{-}$ show a decreasing trend as the number of F-T cycles rises, with values of 0.62%, 0.53%, 0.42%, and 0.35%.

(4) The uniaxial cyclic loading and unloading procedure has changed. The ringing count of rock specimens can be separated into an increasing stage, a slow decreasing stage, and a steep increasing stage. The number of rings in the growth stage is greater, and the duration is shorter. The ringing count rises with loading and falls with unloading during the slow-down phase. During the initial loading and unloading cycle, the cumulative ringing count reached its highest value and then progressively dropped to a stable level. In the steep rise stage, there was a brief AE signal silence interval that can serve as a precursor criterion for predicting the sudden breakdown of rocks.

(5) The type of microcracks inside the rock specimen was determined in the first cycle of loading and unloading, and the distribution of RA and AF in the subsequent loading and unloading process was basically consistent with that in the first cycle. The internal microcracks in red sandstone indicate that shear fractures predominate in shear failure and tensile cracks predominate in tensile failure as the number of F-T cycles rises.

Author Contributions: Data curation, Writing—original draft, Supervision, Funding acquisition, C.Y.; Conceptualization, Writing—original draft, Visualization, Validation, Software, S.H.; Formal analysis, J.L.; Supervision, Funding acquisition, X.W.; Methodology, Software, Y.T.; Supervision, Methodology, X.B. All authors have read and agreed to the published version of the manuscript.

Data Availability Statement: The datasets generated and/or analyzed during the current study are not publicly available due to privacy restrictions but are available from the corresponding author upon reasonable request.

Conflicts of Interest: The authors declare no conflicts of interest.

References

1. Zheng, Y.; Chen, C.X.; Liu, T.T.; Zhang, H.N.; Sun, C.Y. Theoretical and numerical study on the block-flexure toppling failure of rock slopes. *Eng. Geol.* **2019**, *263*, 105293–105309. [CrossRef]
2. Zhou, R.C. Predictive acoustical behavior of rockburst phenomena in Gaoligongshan tunnel, Dulong river highway, China. *Eng. Geol.* **2018**, *247*, 117–128. [CrossRef]
3. Liu, Y.; Dai, F. A review of experimental and theoretical research on the deformation and failure behavior of rocks subjected to cyclic loading. *J. Rock Mech. Geotech. Eng.* **2021**, *13*, 1203–1230. [CrossRef]
4. Xiao, W.J.; Yu, G.; Li, H.T.; Zhan, W.Y.; Zhang, D.M. Experimental study on the failure process of sandstone su-bjected to cyclic loading and unloading after high temperature treatment. *Eng. Geol.* **2021**, *293*, 106305–106320. [CrossRef]
5. Zhang, H.; Huang, L.; Li, X.; Hu, X.; Wu, Y. Study on the Evolution of Physical Parameters and Dynamic Com-pression Mechanical Properties of Granite after Different Heating and Cooling Cycles. *Materials* **2023**, *16*, 2300. [CrossRef] [PubMed]
6. Shen, R.; Chen, T.; Li, T.X.; Li, H.R.; Zhang, X. Study on the effect of the lower limit of cyclic stress on the mechanical properties and acoustic emission of sandstone under cyclic loading and unloading. *Theor. Appl. Fract. Mech.* **2020**, *108*, 102661. [CrossRef]
7. Wang, P.; Xu, J.Y.; Liu, S.; Wang, H.Y.; Liu, S.H. Static and dynamic mechanical properties of sedimentary rock after freeze-thaw or thermal shock weathering. *Eng. Geol.* **2016**, *210*, 148–157. [CrossRef]
8. Jin, X.; Hou, C.; He, J.; Dias, D. Investigation of the Multi-Scale Deterioration Mechanisms of Anhydrite Rock Ex-posed to Freeze–Thaw Environment. *Materials* **2024**, *17*, 726. [CrossRef] [PubMed]
9. Xiao, W.J.; Zhang, D.M.; Wang, X.J. Experimental study on progressive failure process and permeability characte-ristics of red sandstone under seepage pressure—ScienceDirect. *Eng. Geol.* **2019**, *265*, 105406. [CrossRef]
10. Yu, C.Y.; Tang, S.B.; Tang, C.A.; Duan, D.; Zhang, Y.J.; Liang, Z.Z.; Ma, K.; Ma, T.H. The effect of water on the creep behavior of red sandstone. *Eng. Geol.* **2019**, *253*, 64–74. [CrossRef]
11. Li, X.W.; Yao, Z.S.; Huang, X.W.; Liu, Z.X.; Zhao, X.; Mu, K.H. Investigation of deformation and failure characteristics and energy evolution of sandstone under cyclic loading and unloading. *Rock Soil Mech.* **2021**, *42*, 1693–1704. [CrossRef]
12. Qin, L.; Liu, P.; Wang, H.; Li, B.; Wang, R.; Li, J.; Luo, R.; Lv, S. Mechanical Characterization of the Frozen and Thawed States of Coal after the Action of LN_2 at In Situ Formation Pressure. *Processes* **2024**, *12*, 299. [CrossRef]
13. Wang, Y.; Wang, H.; Tao, S.; Yi, X. On the Dynamic Mechanical Behaviors of a Fault Unwelded Bimrock Exposed to Freeze-Thaw-Fatigue Loads: A Lab-Scale Testing. *Geofluids* **2022**, *2022*, 7851201. [CrossRef]

14. Mousavi, S.Z.S.; Tavakoli, H.; Moarefvand, P.; Rezaei, M. Assessing the effect of freezing-thawing cycles on the results of the triaxial compressive strength test for calc-schist rock. *Int. J. Rock Mech. Min. Sci.* **2019**, *123*, 104090. [CrossRef]

15. Cao, R.H.; Wang, C.S.; Yao, R.B.; Hu, T.; Lei, D.X.; Lin, H.; Zhao, Y.L. Effects of cyclic freeze-thaw treatments on the fracture characteristics of sandstone under different fracture modes: Laboratory testing. *Theor. Appl. Fract. Mech.* **2020**, *109*, 102738. [CrossRef]

16. Wang, Y.; Gao, S.H.; Liu, D.Q.; Li, C.H. Anisotropic fatigue behaviour of interbeded marble subjected to uniaxial cyclic compressive loads. *Fatigue Fract. Eng. Mater. Struct.* **2020**, *43*, 1170–1183. [CrossRef]

17. Wang, Y.; Feng, W.K.; Li, C.H. On anisotropic fracture and energy evolution of marble subjected to triaxial fatig-ue cyclic-confining pressure unloading conditions. *Int. J. Fatigue* **2020**, *134*, 105524. [CrossRef]

18. Momeni, A.; Abdilor, Y.; Khanlari, G.R.; Heidari, M.; Sepahi, A. The effect of freeze–thaw cycles on physical and mechanical properties of granitoid hard rocks. *Bull. Eng. Geol. Environ.* **2016**, *75*, 1649–1656. [CrossRef]

19. Zhang, H.M.; Yang, G.S.; Liang, Y. Experimental Study on Damage Deterioration and Tensile Characteristics of Rock under Freeze-Thaw Environment. *Adv. Mater. Res.* **2012**, *518–523*, 1749–1752. [CrossRef]

20. Chen, G.Q.; Jian, D.; Chen, Y.H.; Wan, Y.; Lin, Z.H. Shear creep characteristics of red sandstone after freeze-thaw with different water contents. *Chin. J. Geotech. Eng.* **2021**, *43*, 661–669. [CrossRef]

21. Lu, X.; Zhou, W.; Cai, Q.X.; Li, M.; Luan, B.Y.; Liu, F.M. Mechanical properties and meso fracture mechanism of mudstone under freeze-thaw cycle. *J. Min. Saf. Eng.* **2021**, *38*, 11. [CrossRef]

22. Butt, S.D.; Frempong, P.K.; Mukherjee, C.; Upshall, J. Characterization of the permeability and acoustic properties of an outburst-prone sandstone. *J. Appl. Geophys.* **2005**, *58*, 1–12. [CrossRef]

23. Kramadibrata, S.; Simangunsong, G.M.; Shimada, M.H. Role of Acoustic Emission for Solving Rock Engineering Problems in Indonesian Underground Mining. *Rock Mech. Rock Eng.* **2011**, *44*, 282–289. [CrossRef]

24. Zhang, S.W.; Lin, H.; Chen, Y.F.; Wang, Y.X.; Zhao, Y.L. Acoustic emission and failure characteristics of cracked rock under freezing-thawing and shearing. *Theor. Appl. Fract. Mech.* **2022**, *121*, 103532–103537. [CrossRef]

25. Li, D.X.; Wang, E.Y.; Xiang Guo, K.; Jia, H.S.; Wang, D.M.; Muhammad, A. Damage precursor of construction rocks under uniaxial cyclic loading tests analyzed by acoustic emission. *Constr. Build. Mater.* **2019**, *206*, 169–178. [CrossRef]

26. Song, Y.Q.; Ma, H.F.; Liu, J.C.; Li, X.S.; Zheng, J.J.; Fu, H. Experimental investigation on the damage characteristics of freeze-thaw limestone by the uniaxial compression and acoustic emission monitoring tests. *Chin. J. Rock Mech. Eng.* **2022**, *41*, 2603–2614. [CrossRef]

27. Chu, Y.P.; Zhang, D.M.; Liu, H.; Wu, X.Y.; Zhai, P.; Sheng, T. Experimental study on mechanical properties, acoustic emission characteristics and energy evolution of coal samples after freezing with liquid nitrogen. *Fuel* **2022**, *321*, 123955. [CrossRef]

28. Feng, Q.; Jin, J.C.; Zhang, S.; Liu, W.W.; Yang, X.X.; Li, W.T. Study on a Damage Model and Uniaxial Compressi-on Simulation Method of Frozen–Thawed Rock. *Rock Mech. Rock Eng.* **2022**, *55*, 187–211. [CrossRef]

29. Zhang, H.M.; Yang, G.S. Research on damage model of rock under coupling action of freeze-thaw and load. *Chin. J. Rock Mech. Eng.* **2010**, *29*, 471–476.

30. Wang, Y.; Li, C.H.; Han, J.Q.; Wang, H.J. Mechanical behaviours of granite containing two flaws under uniaxial increasing-amplitude fatigue loading conditions: An insight into fracture evolution analyses. *Fatigue Fract. Eng. Mater. Struct.* **2020**, *43*, 2055–2070. [CrossRef]

31. Wang, Y.; Gao, S.H.; Li, C.H.; Han, J.Q. Investigation on fracture behaviors and damage evolution modeling of freeze-thawed marble subjected to increasing-amplitude cyclic loads. *Theor. Appl. Fract. Mech.* **2020**, *109*, 102679. [CrossRef]

32. Ulusay, R. The ISRM Suggested Methods for Rock Characterization, Testing and Monitoring: 2007–2014. In *The Present and Future of Rock Testing: Highlighting the ISRM Suggested Methods*; Springer: Berlin/Heidelberg, Germany, 2015; pp. 1–22. [CrossRef]

33. Khanlari, G.; Sahamieh, R.Z.; Abdilor, Y. The effect of freeze–thaw cycles on physical and mechanical properties of Upper Red Formation sandstones, central part of Iran. *Arab. J. Geosci.* **2014**, *8*, 5991–6001. [CrossRef]

34. Ghobadi, M.H.; Babazadeh, R. Experimental Studies on the Effects of Cyclic Freezing-Thawing, Salt Crystallization, and Thermal Shock on the Physical and Mechanical Characteristics of Selected Sandstones. *Rock Mech. Rock Eng.* **2015**, *48*, 1001–1016. [CrossRef]

35. Liu, H.; Lin, J.H.; Yang, G.S.; Yun, Y.H.; Zhang, H.M.; Liang, B.; Zhang, Y. Acoustic emission test on tensile damage characteristics of sandstone under freeze-thaw cycle. *J. Min. Saf. Eng.* **2021**, *38*, 830–839. [CrossRef]

36. Liu, Y.Z.; Cai, Y.T.; Huang, S.B.; Guo, Y.L.; Liu, G.F. Effect of water saturation on uniaxial compressive strength and damage degree of clay-bearing sandstone under freeze-thaw. *Bull. Eng. Geol. Environ.* **2019**, *74*, 2021–2036. [CrossRef]

37. Niu, C.Y.; Zhu, Z.M.; Zhou, L.; Li, X.H.; Deng, S. Study on the microscopic damage evolution and dynamic fract-ure properties of sandstone under freeze-thaw cycles. *Cold Reg. Sci. Technol.* **2021**, *191*, 103328. [CrossRef]

38. Li, T.; Ma, Y.J.; Liu, B.; Sheng, H.L.; He, P. Strength characteristics and elastic modulus evolution of frozen gray sandstone under cyclic loading. *J. China Coal Soc.* **2018**, *43*, 2438–2443. [CrossRef]

39. Fu, H.L.; Li, H.; Li, J.; Hu, K.X. Research on freezing-dynamic combined damage characteristics of carbonaceous phyllite in cold region. *J. China Coal Soc.* **2023**, 1–12. [CrossRef]

40. Wu, Q.; Li, B.; Jiang, X. Triaxial Test Study on Energy Evolution of Marble after Thermal Cycle. *Minerals* **2023**, *13*, 428. [CrossRef]

41. Cui, Y.; Xue, L.; Zhai, M.Y.; Xu, C.; Bu, F.C.; Wan, L. Experimental investigation on the influence on mechanical properties and acoustic emission characteristics of granite after heating and water-cooling cycles. *Geomech. Geophys. Geo-Energy Geo-Resour.* **2023**, *9*, 88. [CrossRef]

42. Huq, F.; Liu, J.; Tonge, A.L.; Graham-Brady, L. A micromechanics based model to predict micro-crack coalescence in brittl-e materials under dynamic compression. *Eng. Fract. Mech.* **2019**, *217*, 106515. [CrossRef]
43. Martin, C.D.; Chandler, N.A. The progressive fracture of Lac du Bonnet granite. *Int. J. Rock Mech. Min. Sci. Geomech. Abstr.* **1994**, *31*, 643–659. [CrossRef]
44. Luo, Z.S.; Zhu, Z.X.; Bai, H.; Liu, D.X.; Sun, Q.C. Research on the Influence of Moisture Condition on the Mechanical Properties and Microstructure of Sandstone. *Shock. Vib.* **2021**, *2021*, 4850650. [CrossRef]
45. Yin, Q.; Zhu, C.; Wu, J.; Pu, H.; Wang, Q.; Zhang, Y.; Jing, H.; Deng, T. Shear sliding of rough-walled fracture surfaces under unloading normal stress. *J. Rock Mech. Geotech. Eng.* **2023**, *15*, 2658–2675. [CrossRef]
46. Seok, H.J.; In, L.C.; Kwon, J.S. Measurement of Acoustic Emission and Source Location Considering Anisotropy of Rock under Triaxial Compression. *Key Eng. Mater.* **2004**, *270–273*, 1574–1579. [CrossRef]
47. Yin, Q.; Nie, X.; Wu, J.; Wang, Q.; Bian, K.; Jing, H. Experimental study on unloading induced shear performances of 3D saw-tooth rock fractures. *Int. J. Min. Sci. Technol.* **2023**, *33*, 463–479. [CrossRef]
48. Su, Z.D.; Sun, J.Z.; Xia, J.; Wu, C.L. Experimental research of the effect of freezing-thawing cycles on acoustic e-mission characteristics of granite. *Chin. J. Rock Mech. Eng.* **2019**, *38*, 865–874. [CrossRef]
49. Niu, Y.; Zhou, X.P.; Berto, F. Evaluation of fracture mode classification in flawed red sandstone under uniaxial co-mpression. *Theor. Appl. Fract. Mech.* **2020**, *107*, 102512–102528. [CrossRef]